PNAS

Supporting Information for

Dissolved gases in the deep North Atlantic track ocean ventilation processes

Alan M. Seltzer*, David P. Nicholson, William M. Smethie, Rebecca L. Tyne, Emilie Le Roy, Rachel H.R. Stanley, Martin Stute, Peter H. Barry, Katelyn McPaul, Perrin W. Davidson, Bonnie X. Chang, Patrick A. Rafter, Paul Lethaby, Rod J. Johnson, Samar P. Khatiwala, William J. Jenkins

Corresponding Author: Alan Seltzer
Email: aseltzer@whoi.edu

This PDF file includes:

Figures S1 to S17
Tables S1 to S2

Other supporting materials for this manuscript include the following:

Dataset S1

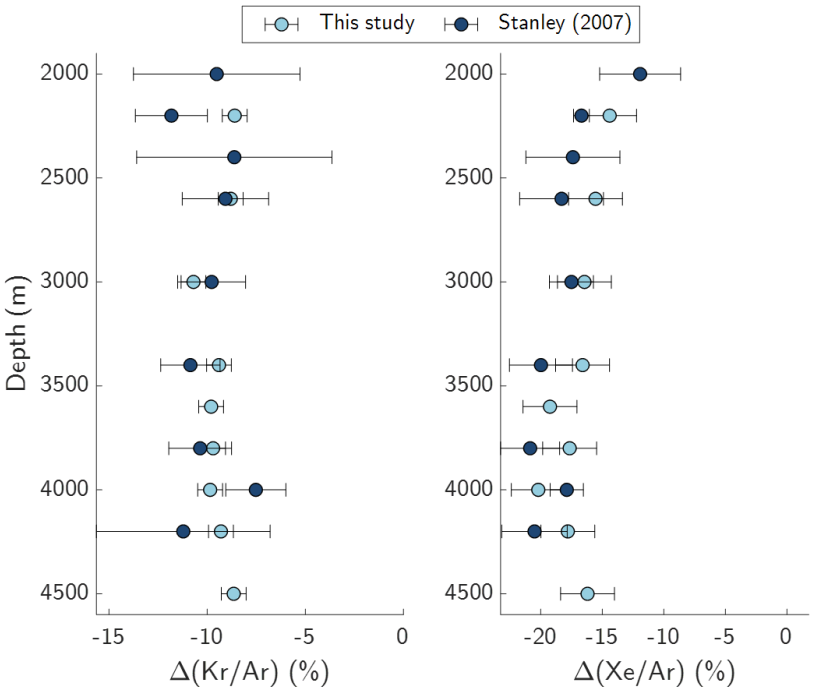

Figure S1: Comparison of deep BATS Kr/Ar and Xe/Ar solubility disequilibrium measured in this study and by Stanley et al. (2007). Given the large number of measurements in Stanley et al. (2007), from 2002-2005, here we show binned 200-m averages from 2000-m and below. For new data from this study, each marker represents a mean of two measurements made on replicate deep casts. Note that erroneously low Kr data are discarded (where Δ(Kr/Ar) is below -20‰, due to analytical artifacts described in Stanley et al. (2007)). Error bars indicate ±2 standard errors of the mean for each depth bin.

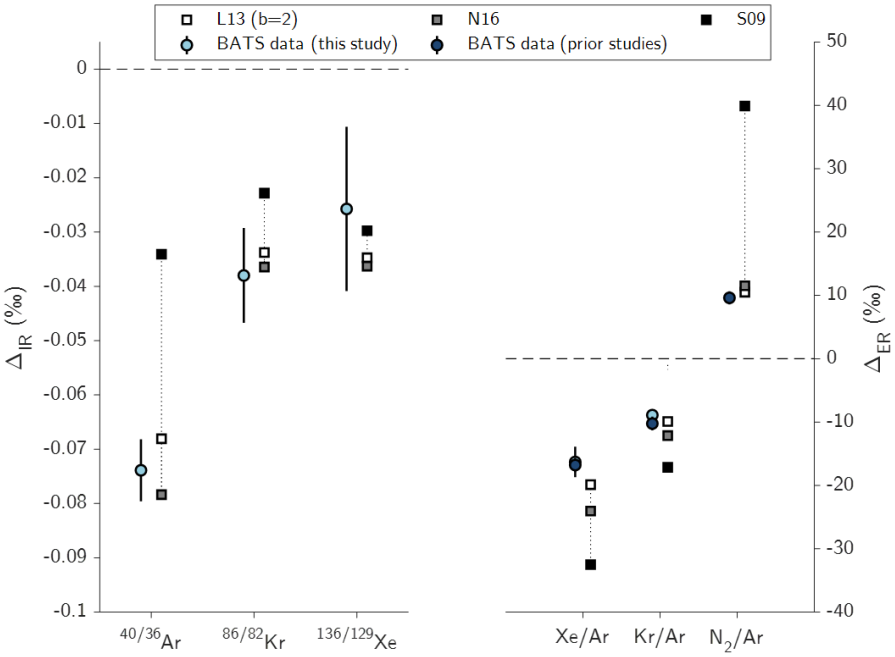

Figure S2: Comparison of deep BATS measurements (>2 km) to model simulations using three different gas exchange models: Liang et al. (2013) (L13) with bubble fluxes enhanced by a factor of 2.0, Nicholson et al. (2016) (N16), and Stanley et al. (2009) (S09). We find the bubble-enhanced Liang et al. (2013) displays the closest agreement with measurements from the deep ocean at BATS. All models appear to underestimate Δ(Xe/Ar), which we suggest likely stems from the much larger sensitivity of Δ(Xe/Ar) to diapycnal mixing, owing to the high curvature of the Xe solubility function (with respect to temperature), as well as the larger vertical gradients in ΔXe. Since diapycnal mixing acts to increase Δ(Xe/Ar), the low bias of all simulations in principle suggests that the UVic ESCM has lower rates of diapycnal mixing than reality.

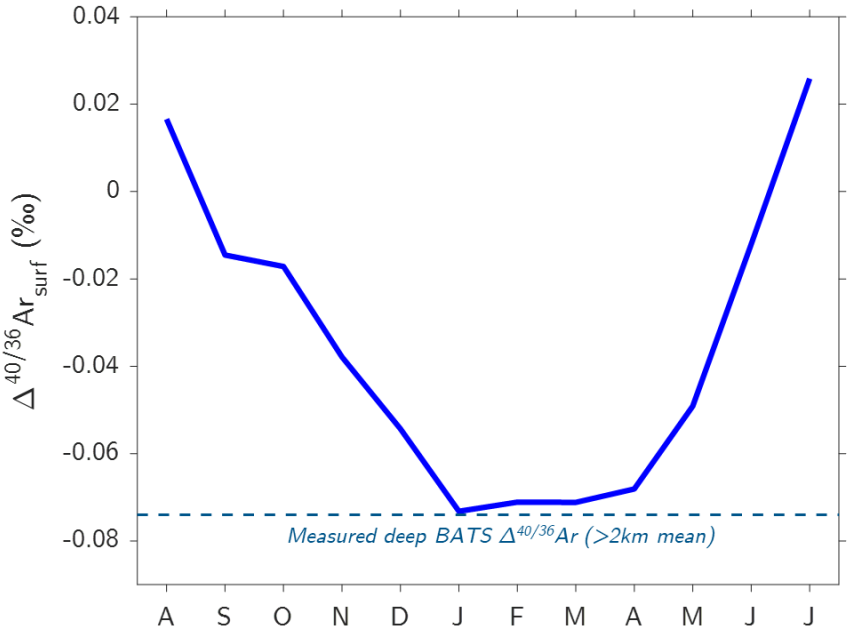

Figure S3: Simulated seasonal cycle of Ar isotope disequilibrium in the surface (0-35 m) of the Irminger Sea (60-65ºN, 30-40ºW), in TMM simulations of the UVic ESCM coupled to the L13 gas exchange parameterization with doubled bubble fluxes (b=2 in Eq. 2). The x-axis indicates month of year, from August through July. The dashed line indicates the observed deep-ocean (>2 km) mean Ar isotope disequilibrium at BATS.

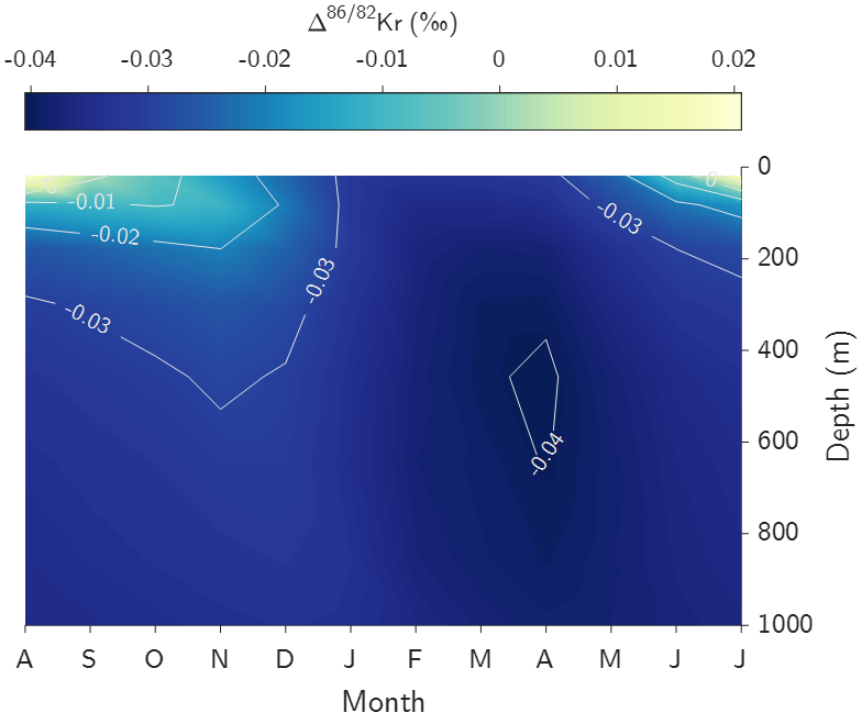

Figure S4: Simulated seasonal evolution of Kr isotope solubility disequilibrium ($\Delta^{86/82}Kr$) in the Irminger Sea (area-weighted mean of model grid cells between 60-65ºN and 30-40ºW). Bottom axis tick labels are month name abbreviations consecutively from August through July. All other details are the same as described in the caption to Fig. 3.

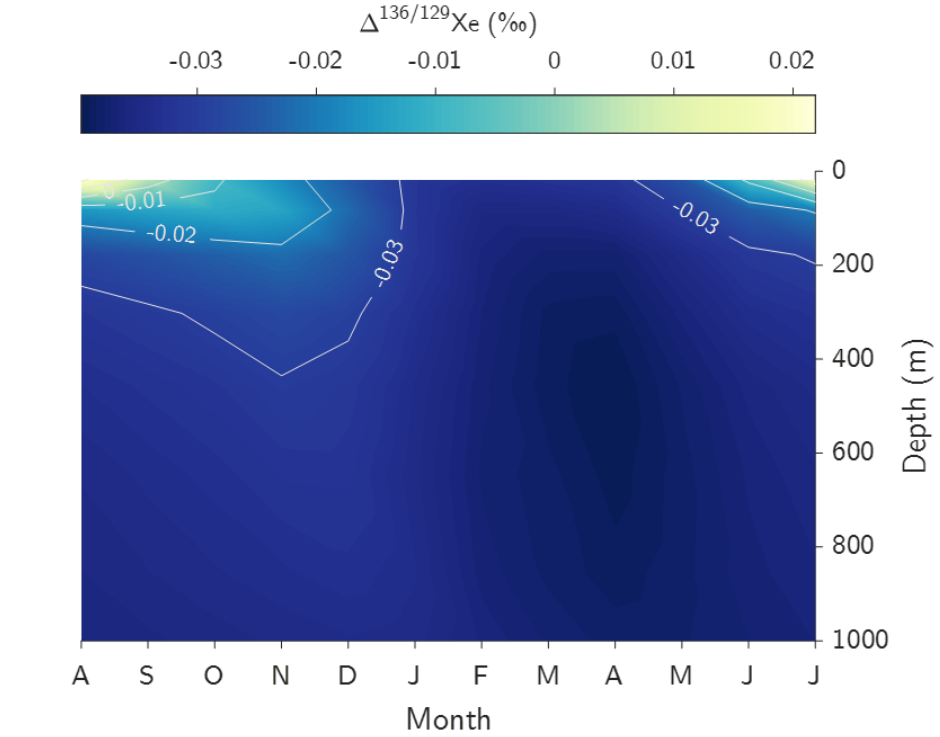

Figure S5: Simulated seasonal evolution of Xe isotope solubility disequilibrium ($\Delta^{136/129}$Xe) in the Irminger Sea (area-weighted mean of model grid cells between 60-65ºN and 30-40ºW). Bottom axis tick labels are month name abbreviations consecutively from August through July. All other details are the same as described in the caption to Fig. 3.

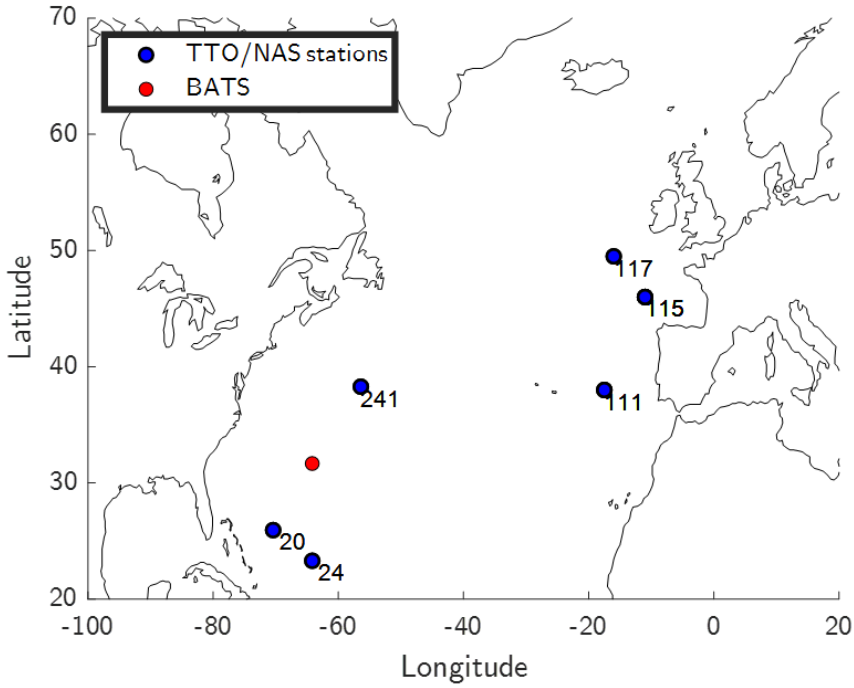

Figure S6: Map of TTO/NAS station locations (blue markers with annotated station numbers) and BATS site (red marker).

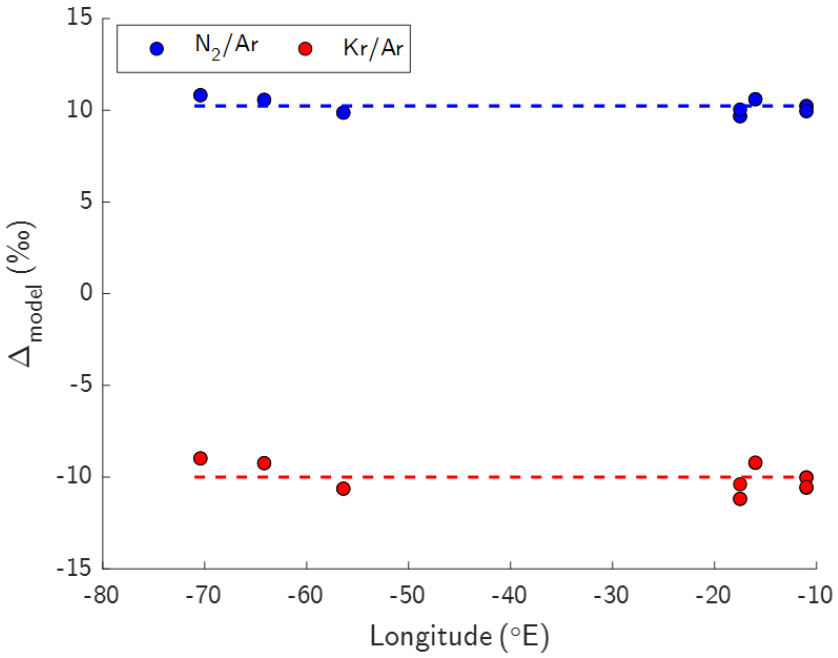

Figure S7: Simulated Δ(Kr/Ar) and Δ(N_2/Ar) in the deep North Atlantic, at the locations of TTO/NAS samples analyzed in this study. Shown here are the nearest grid cells in the model (UVic ESCM with L13 gas exchange parameterization, b=2) to TTO/NAS sampling locations.

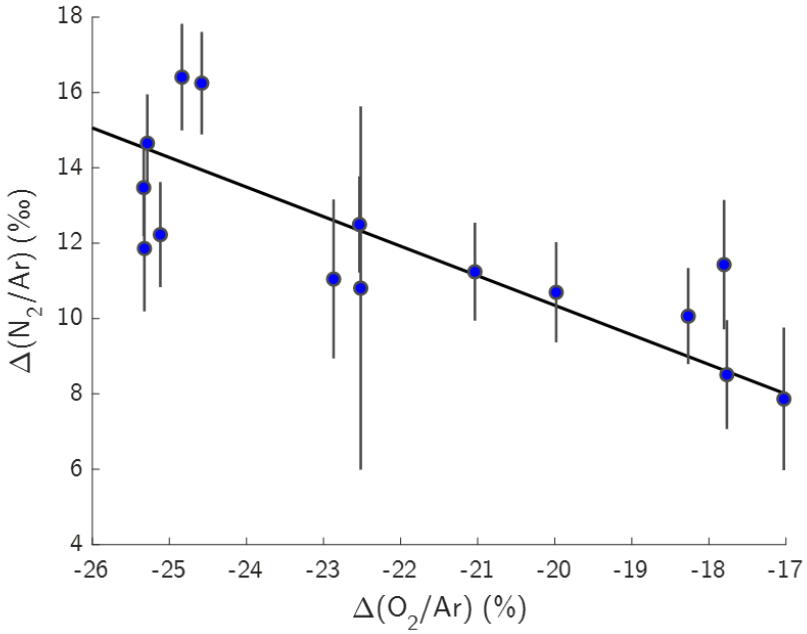

Figure S8: Comparison of Δ(N_2/Ar) and Δ(O_2/Ar) across analyses of 15 deep North Atlantic TTO/NAS tanks. Δ(N_2/Ar) is corrected for physical fractionation (see Materials and Methods), and Δ(O_2/Ar) does not require a correction because of the similar colligative properties of O_2 and Ar, and the fact that the scale of actual Δ(O_2/Ar) variability is much larger than any physical artifacts. The linear trend (reduced major axis regression) is consistent with benthic denitrification, as the deep ocean should lose O_2 and gain N_2 from exchange with low-O_2 sediment pore waters in which denitrification takes place. Δ(O_2/Ar) error bars are smaller than marker size.

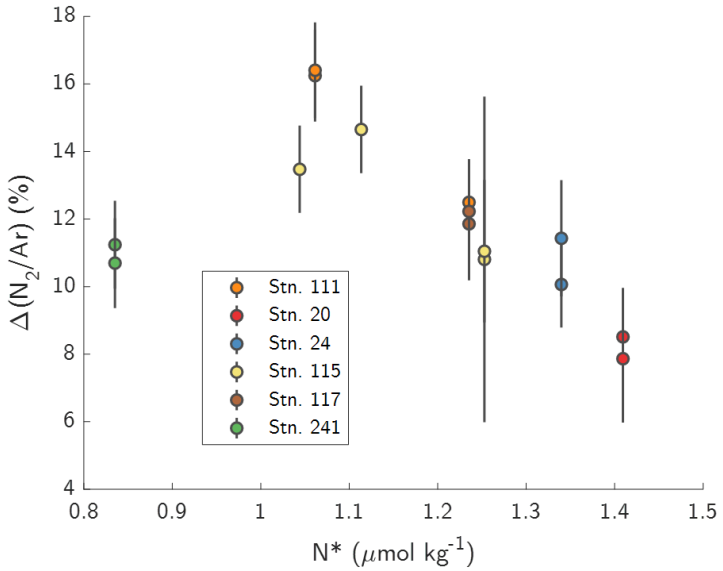

Figure S9: Comparison of $\Delta(N_2/Ar)$ to N* for 15 deep-ocean TTO/NAS samples. N* is defined here as 0.87 x ($[NO_3^-]$ – $[PO_4^{3-}]$ + 2.9) following Gruber and Sarmiento (1997), using bottle data from the TTO/NAS cruises in 1981. Lower N* indicates greater loss of fixed N. Station 241 appears to exhibit anomalously low N* in the depth range of our samples (see Fig. S10).

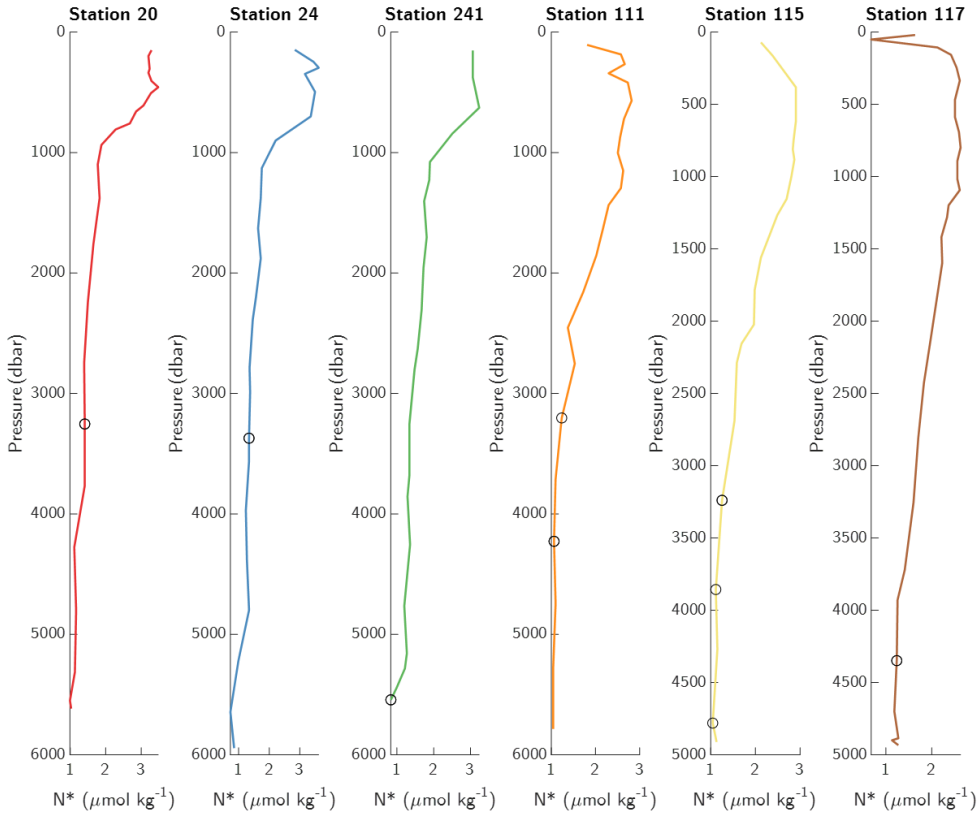

Figure S10: Profiles of N* from the TTO/NAS bottle data analyzed in 1981. Lower N* indicates greater loss of fixed N. Open circles indicate sampling locations for samples included in this study. Station 241 appears to exhibit a localized low N* anomaly in the vicinity of the replicate samples analyzed in this study.

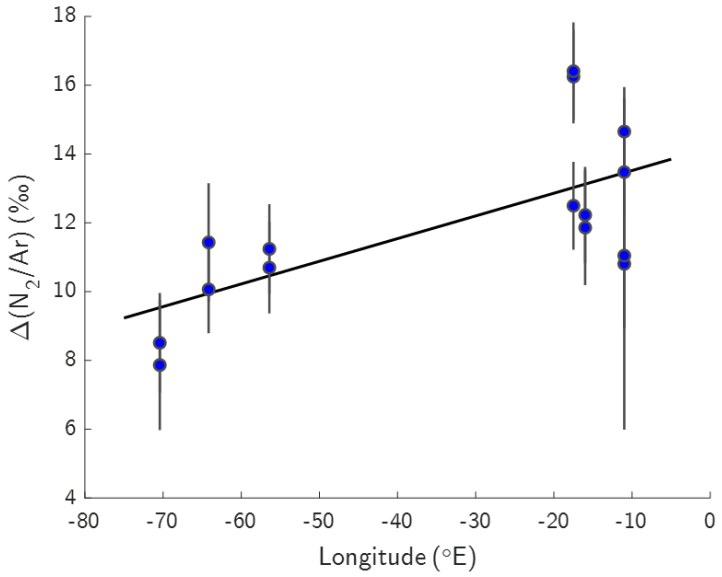

Figure S11: TTO/NAS tank $\Delta(N_2/Ar)$ versus sample longitude. The positive linear trend (ordinary least squares regression) is consistent with gradual accumulation of excess N_2 from benthic denitrification in older deep waters within the eastern North Atlantic.

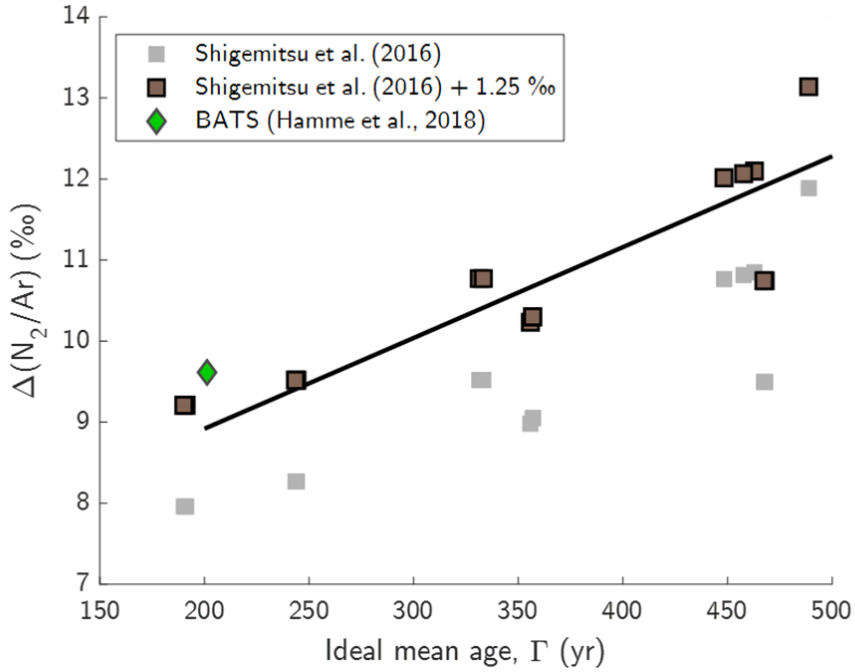

Figure S12: Evaluation of $\Delta(N_2/Ar)$ in the biogeochemical model of Shigemitsu et al. (2016) at model grid locations nearest to each of the 15 TTO/NAS samples, against ideal mean age estimates at these same locations from the inverse model estimates of Khatiwala et al. (2012) and Holzer et al. (2021). We correct the Shigemitsu et al. (2016) data for the ~1.25‰ offset from observations, as shown in the original paper. Here, the mean of the two inverse model age estimates is used, and the trendline (reduced major axis regression) suggests an average rate of $\Delta(N_2/Ar)$ increase of 11.2 ‰ kyr^{-1}. In absolute terms, for deep ocean waters (θ≈2ºC; S≈35), a 1‰ excess in N_2/Ar corresponds to ~0.6 μmol_{N2} kg^{-1} or ~1.2μmol_N kg^{-1}. Thus, a 11.2 ‰ kyr^{-1} rate of excess N_2 accumulation corresponds to ~13.3 μmol_N kg^{-1} kyr^{-1}. As an illustrative example, if integrated over the North Atlantic ocean below 3 km (equator to 66ºN; M≈$3.1x10^{19}$kg), this would correspond to a benthic denitrification rate of ~5.9 TgN yr^{-1}, which is roughly one third of the non-shelf (>150 m) benthic denitrification in the North Atlantic suggested by Bianchi et al. (2012). Integrated over the entire deep ocean below 3 km (M≈$3.0x10^{20}$kg), the corresponding rate of benthic denitrification would be ~56 TgN yr^{-1}, which is more than one quarter of global benthic denitrification (51), and much greater than the ~10% of global benthic denitrification suggested to occur below 3 km (51). This points towards the high regional rate of benthic denitrification (i.e., higher than global mean) in the deep North Atlantic, consistent with the high POC flux to sediments (54).

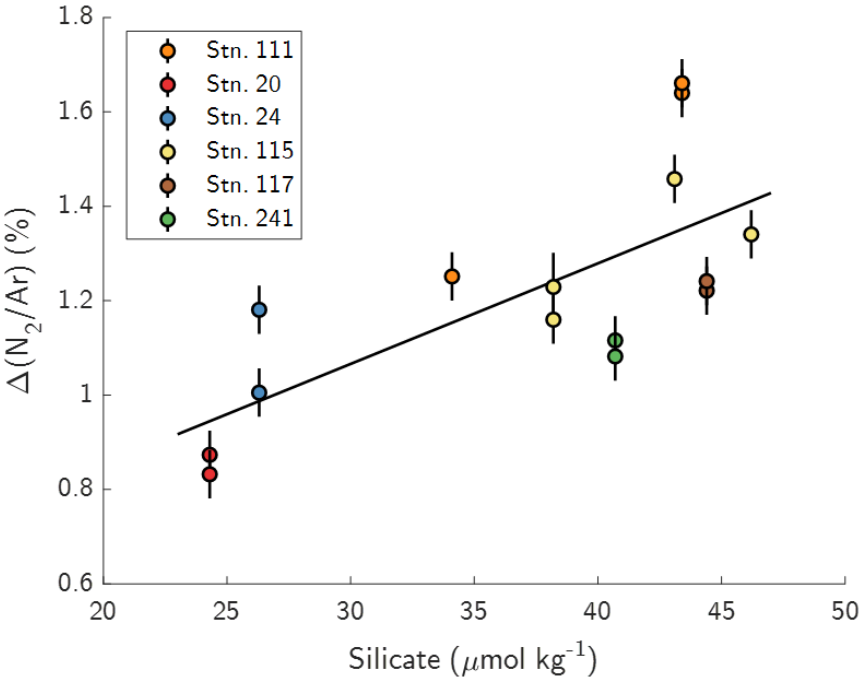

Figure S13: Positive trend in $\Delta(N_2/Ar)$ versus silicate (from 1981 TTO/NAS bottle data; reduced major axis regression) suggests that $\Delta(N_2/Ar)$ may in part be linked to a greater contribution of southern sourced deep waters in the eastern North Atlantic, since Antarctic Bottom Water (AABW) has characteristically high silica content (28). As discussed in the main text, we suggest that elevated $\Delta(N_2/Ar)$ in AABW may ultimately explain ~1‰ of the observed eastern-western deep North Atlantic $\Delta(N_2/Ar)$ difference. (Note that measurement uncertainties on 1981 silicate data are unavailable.)

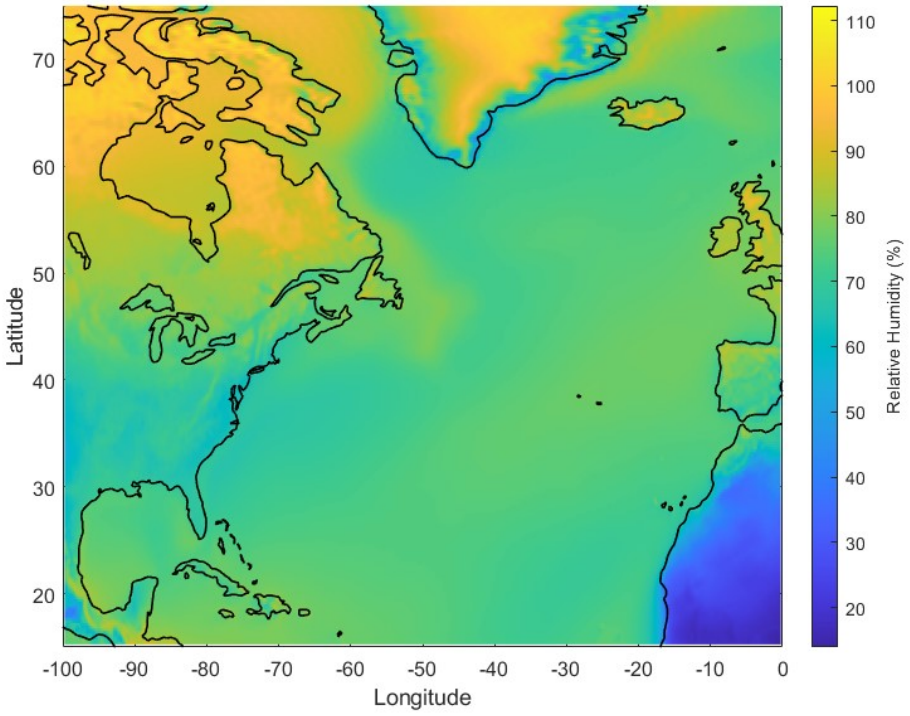

Figure S14: Mean November-through-March near-surface relative humidity in the North Atlantic, from ERA5 reanalysis data averaged from 1959-2021 (59).

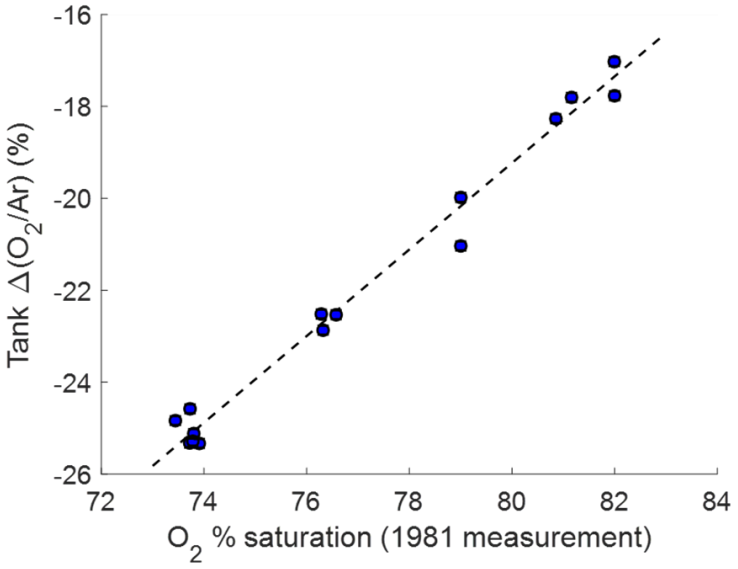

Figure S15: Comparison of oxygen content analyzed in aliquots of stored TTO/NAS tanks with original at-sea O_2 measurements in 1981. $\Delta(O_2/Ar)$ should be ~equal to O_2 saturation minus 100%, since O_2 and Ar have similar colligative properties and O_2 is consumed with the ocean interior while Ar is a conservative tracer. The close agreement between measured O_2/Ar in tank aliquots and 1981 at-sea measurements confirms the integrity of these stored dissolved gas samples. (Note that error in $\Delta(O_2/Ar)$ is roughly the size of marker samples and no error estimates were provided for 1981 at-sea O_2 data.)

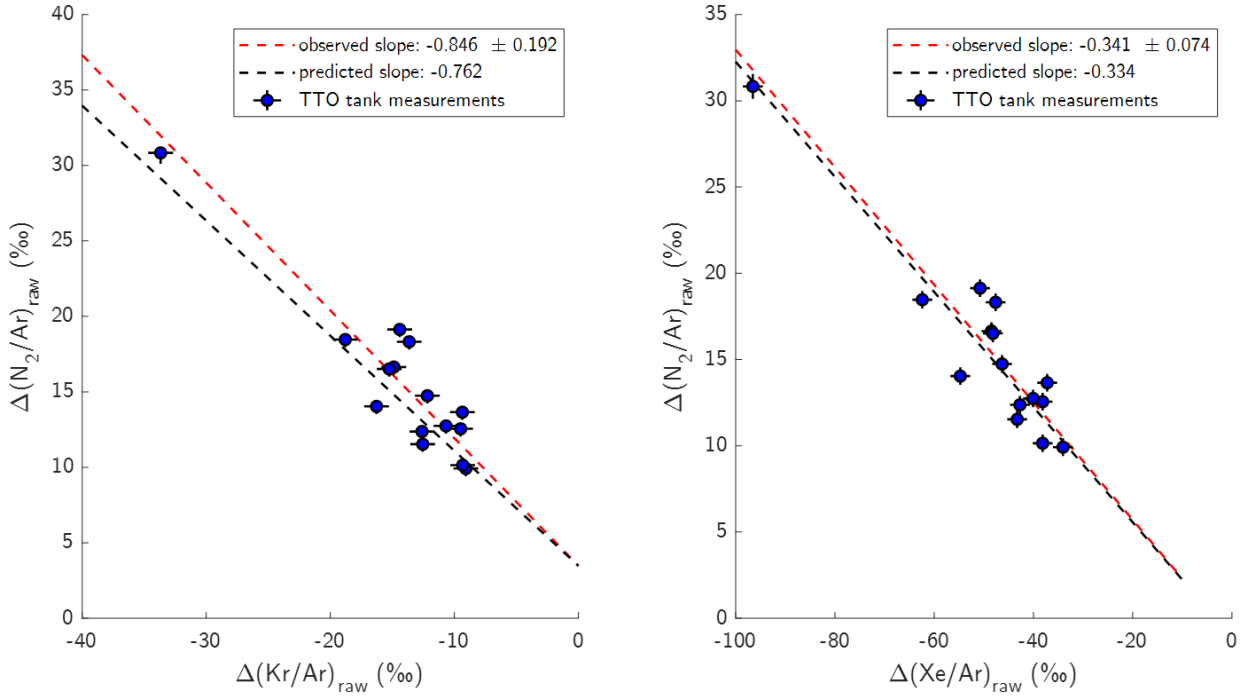

Figure S16: Physical fractionation of Kr/Ar (left panel), Xe/Ar (right panel, and N_2/Ar (both panels) due to incomplete extraction at sea in 1981 during TTO/NAS sample collection leads to an increase in apparent $\Delta(N_2/Ar)$ and decrease in apparent $\Delta(Xe/Ar)$ due to solubility and diffusivity differences among these gases, as described in the Materials and Methods. The subscript "raw" indicates that these data are uncorrected for physical fractionation. The observed slope is remarkably close to the predicted slope based on diffusivity and solubility differences of Ar, Xe, and N_2, using a simple diffusive degassing model. The similar agreement between observed and predicted slopes between $\Delta(Xe/Ar)$ and $\Delta(N_2/Ar)$, and $\Delta(Kr/Ar)$ and $\Delta(N_2/Ar)$, adds confidence to the physical correction scheme.

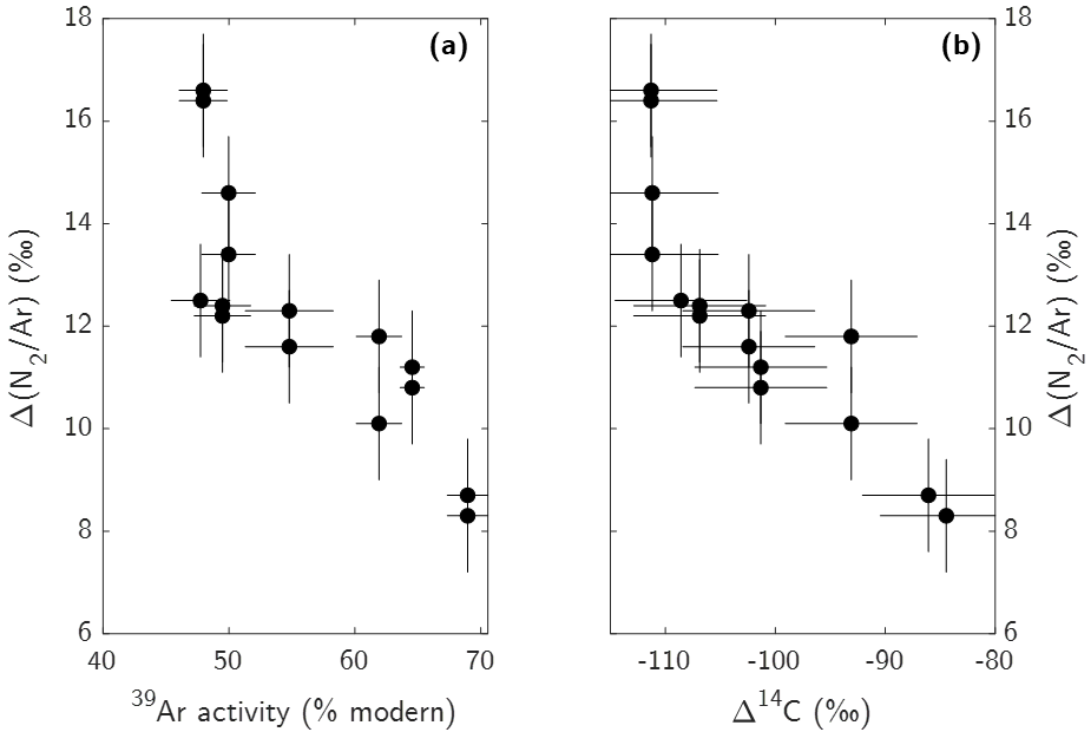

Figure S17: Comparison of TTO/NAS $\Delta(N_2/Ar)$ to age tracer activities from OCIM2 evaluated at sample locations (26, 27). The anticorrelation between $\Delta(N_2/Ar)$ and ^{39}Ar (panel a) and ^{14}C (panel b) are consistent with the notion that high $\Delta(N_2/Ar)$ reflects greater accumulation of N_2 in older deep waters.

Table S1: Comparison of gas exchange fluxes for O_2 among leading bubble-mediated gas exchange parameterizations for a hypothetical scenario of 20 m s^{-1} winds (10 m above surface), 2 ºC upper ocean temperature, 35 psu salinity, and an initial oxygen undersaturation, ΔO_2, of -3% driving diffusive exchange. F_{net}, F_S, F_C, and F_P refer to net air-sea gas exchange, surface diffusive exchange, complete bubble dissolution, and partial bubble dissolution, respectively, as described in the main text. All fluxes are reported in µmol m^{-2} s^{-1}.

Parameterization	F_{net}	F_S	F_C	F_P	Reference
L13 (b=2)	16.2	1.4	2.8	11.9	(23)
L13 (b=1)	8.8	1.4	1.4	6.0	(23)
N16	5.3	3.9	1.2	0.1	(15)
S09	10.5	4.4	4.7	1.4	(37)

Table S2: Comparison of solubilities (henry coefficient, *K*) of gases in seawater (T=2ºC; S=35) as indication of relative sensitivities to bubble fluxes. Values are given in 10^{-2} mol kg^{-1} atm^{-1} (such that the equilibrium concentration [mol kg^{-1}] of a dissolved gas could be calculated from its dry gas pressure [atm] in air above the sea surface).

Gas	K (10^{-2} mol kg^{-1} atm^{-1})	Reference
O_2	1.6	(64)
CO_2	58.2	(65)
SF_6	0.4	(66)
N_2	0.8	(61)
CFC-11	23.3	(67)
CFC-12	5.8	(67)
Ne	0.4	(21)
Ar	1.7	(21)
Kr	3.5	(21)
Xe	6.9	(21)